OPEN ACCESS



Evidence of a Massive Stellar Disruption in the X-Ray Spectrum of ASASSN-14li

Jon M. Miller b, Brenna Mockler Benrico Ramirez-Ruiz b, Paul A. Draghis b, Jeremy J. Drake b, John Raymond b, Mark T. Reynolds b, Xin Xiang b, Sol Bin Yun and Abderahmen Zoghbi b, John Raymond b, Mark T. Reynolds b, Xin Xiang b, Sol Bin Yun and Abderahmen Zoghbi b, John Raymond b, Mark T. Reynolds b, Xin Xiang b, Sol Bin Yun and Abderahmen Zoghbi b, John Raymond b, Mark T. Reynolds b, Xin Xiang b, Paul A. Draghis b, Jeremy J. Drake b, John Raymond b, Mark T. Reynolds b, Xin Xiang b, Paul A. Draghis b, Jeremy J. Drake b, John Raymond b, Mark T. Reynolds b, John Raymond b, Mark T. Reynolds b, John Raymond b, Mark T. Reynolds b, John Raymond b, John Raymond b, John Raymond b, Mark T. Reynolds b, John Raymond b,

Abstract

The proximity and duration of the tidal disruption event ASASSN-14li led to the discovery of narrow, blueshifted absorption lines in X-rays and UV. The gas seen in X-ray absorption is consistent with bound material close to the apocenter of elliptical orbital paths, or with a disk wind similar to those seen in Seyfert-1 active galactic nuclei. We present a new analysis of the deepest high-resolution XMM-Newton and Chandra spectra of ASASSN-14li. Driven by the relative strengths of He-like and H-like charge states, the data require $[N/C] \ge 2.4$, in qualitative agreement with UV spectral results. Flows of the kind seen in the X-ray spectrum of ASASSN-14li were not clearly predicted in simulations of TDEs; this left open the possibility that the observed absorption might be tied to gas released in prior active galactic nucleus (AGN) activity. However, the abundance pattern revealed in this analysis points to a single star rather than a standard AGN accretion flow comprised of myriad gas contributions. The simplest explanation of the data is likely that a moderately massive star $(M \gtrsim 3 \, M_{\odot})$ with significant CNO processing was disrupted. An alternative explanation is that a lower mass star was disrupted that had previously been stripped of its envelope. We discuss the strengths and limitations of our analysis and these interpretations.

Unified Astronomy Thesaurus concepts: Black hole physics (159); High energy astrophysics (739)

1. Introduction

Tidal disruption events (TDEs) are observed as multi-wavelength flares when a star is disrupted by a massive black hole (see, e.g., Rees 1988). The ready supply of gas for rapid accretion means that the black hole can briefly accrete in excess of the Eddington limit; this mode of accretion appears to be rare among massive black holes in the nearby universe (e.g., Hickox et al. 2009). The nature and evolution of the accretion flow following a stellar disruption remain a matter of debate; the key questions revolve around how quickly strands of the disrupted star can form an accretion disk, and the relative importance of viscous dissipation, stream collisions, and scattering in producing the radiation that is observed.

These uncertainties are vividly illustrated by comparing the temperatures and emitting areas of the thermal UV and X-ray continua that are simultaneously observed in many TDEs: the temperatures are distinct, and the emitting areas differ by an order of magnitude or more (for reviews, see Roth et al. 2020; Gezari 2021). However, when the thermal X-ray emission from TDEs is fit with a physically motivated model for disk emission, plausible black hole masses are derived (e.g., Mummery & Balbus 2020; Wen et al. 2020, 2023). X-ray observations have also revealed that quasiperiodic oscillations and relativistic reverberation suggest plausible masses (Reis et al. 2012; Kara et al. 2016; Pasham et al. 2019), which is only

Original content from this work may be used under the terms of the Creative Commons Attribution 4.0 licence. Any further distribution of this work must maintain attribution to the author(s) and the title of the work, journal citation and DOI.

possible if at least some of the X-ray flux is direct emission from the innermost accretion flow, rather than scattered light. Optical spectroscopy may also point to rapid circularization and disk formation (e.g., Hung et al. 2020).

Narrow X-ray absorption lines have the potential to trace disk winds, and other structures in the accretion flow that lie close to the central engine. Miller et al. (2015) detected blueshifted absorption lines from moderately and highly ionized charge states of abundant elements in ASASSN-14li. The observed blueshifts, only few $\times 10^2$ km s⁻¹, are similar to those observed in warm absorber winds in nearby Seyfert active galactic nucleus (AGN). It is notable that the outflow speeds are in agreement with UV absorption lines (Cenko et al. 2016). The gas could represent a Seyfert-like wind, or it could represent gas near to the apocenter of elliptical orbits that had not yet formed into a disk. The latter scenario would seem to require a degree of fine-tuning, but the disrupted stars may orbit on paths that are not aligned with the angular momentum of the black hole, potentially creating a kind of "wicker basket" of streams as the TDE unfolds (see, e.g., Guillochon & Ramirez-Ruiz 2015).

ASASSN-14li was discovered with ASASSN on 2014 November 22 (MJD 56983; Jose et al. 2014). It was immediately apparent that the transient coincided with the nucleus of PGC 043234 (also known as Zw VIII 211). At a redshift of just z = 0.0206, or 90.3 Mpc for standard cosmological parameters, ASASSN-14li was the most proximal TDE detected in over 10 yr. Indeed, ASASSN-14li remains the clearest example of a TDE with a wind; its flux also facilitated the detection of X-ray quasiperiodic oscillations that were

stable over many weeks (Pasham et al. 2019), potentially indicating a misalignment of angular momentum vectors. Although ASASSN-14li may be exceptional, it is more likely that these features are detected in this source merely owing to its high X-ray peak flux.

The deep XMM-Newton observation wherein winds were detected is the centerpiece of the new analysis presented herein. The prior fits to the X-ray continuum in that observation with a simple blackbody suggest a black hole mass of $M=2.5\times10^6\,M_\odot$ via Eddington limit scaling, and $M=1.9\times10^6\,M_\odot$ via the implied emitting area (Miller et al. 2015). The early decay of the UV light curve as measured with the Swift/UVM2 filter is consistent with the $F\propto t^{-5/3}$ decay predicted by seminal theory (Rees 1988; Phinney 1989). Assuming this index for the early decay gives a disruption date of $t_0=56948\pm3$. The fits to the full multiwavelength decay with a model including direct and reprocessed emission from an accretion disk gave a mass range of $M=0.4-1.2\times10^6\,M_\odot$ (Miller et al. 2015; also see Guillochon et al. 2014).

In contrast to its early phase, the late evolution of ASASSN-14li between hundreds and 2600 days after the stellar disruption is consistent with a shallow decline or plateau (e.g., van Velzen 2019; Mummery & Balbus 2020; Wen et al. 2020, 2023). The late-time UV spectrum is consistent with an accretion disk, uncomplicated by an additional UV region that may be needed at early times. In particular, when multi-wavelength monitoring data are combined and analyzed within the framework of relativistic disk models, it becomes possible to constrain the total accreted mass (and the disrupted stellar mass, generally taken to be twice the accreted mass following Rees 1988), the mass and spin of the black hole, and potentially the outer radius of the accretion disk and the torque condition at the inner boundary (Mummery & Balbus 2020; Wen et al. 2020, 2023).

Elemental abundances can potentially give an independent angle on the mass of the stars that are disrupted in TDEs. Yang et al. (2017) present an analysis of UV spectra of ASASSN-14li, PTF15af, and iPTF16fnl, and find that $\lceil N/C \rceil \geqslant 1.5$ is required in all cases (also see Cenko et al. 2016 concerning ASASSN-14li). This is consistent with the products of the CNO chain in moderate mass stars, enabling Yang et al. (2017) to place a lower limit of $M \geqslant 0.6\,M_\odot$ on the mass of the disrupted stars in these events. Herein, we reexamine the most sensitive X-ray spectrum of ASASSN-14li, to test if the X-ray data can also be used to constrain abundances and thereby the mass of the disrupted star. Throughout this work, we define $\lceil N/C \rceil$ as the logarithm of the ratio of the abundance of nitrogen relative to its solar value $(A_{\rm C})$.

Section 2 describes the observations and our data reduction. Section 3 presents our analysis and results, using an updated photoionization model. In Section 4, we scrutinize our methods, explore the implications of the inferred N/C abundance ratio, and briefly examine the potential of future X-ray spectroscopy of TDEs.

2. Observations and Reduction

Miller et al. (2015) examined the multiwavelength evolution of ASASSN-14li using the X-ray Telescope (XRT) and UVOT telescopes aboard the Neil Gehrels Swift Observatory. Of the UVOT filters available, the UVM2 has the smallest red leak, and therefore represents the best measure of the UV flux. The

UVM2 light curve is consistent with the anticipated $F \propto t^{-5/3}$ decay, and predicts that the disruption occurred on MJD 56948 \pm 3. The observations that are the focus of this paper started on MJD 56999, approximately 50 days later.

XMM-Newton observation (0722480201) started on 2014 December 8 at 05:38:22 (UT), and obtained 95 ks. The data from the Reflection Grating Spectrometer (RGS) and EPIC cameras were reduced using Scientific Analysis System (SAS) version 1.3 (xmmsas_20211130), and the associated standard calibration files. The RGS was operated in its default *spectroscopy* mode. We generated an EPIC-pn and EPIC-MOS event lists using the tools *epproc* and *emproc*, and used the light curves to create a filter against soft proton flaring. We then ran the tool *rgsproc* to create RGS spectral files, response files, and background files. In order to maximize the sensitivity within the spectra, we restricted our analysis to the time-averaged RGS-1 and RGS-2 spectra.

Chandra observations (17566) and (17567) started on 2014 December 8 at 23:20:28 (UT) and 2014 December 11 at 08:45:20. The total exposures of 34.8 and 44.5 ks were obtained. In both cases, the HRC+LETGS combination was used to obtain high-resolution spectra. CIAO version 4.15 and the associated CALDB files were used to create first-order spectral files, background files, and responses from each observation. These exposures were intended to be a single integration, and the source varied negligibly between the exposures, so we combined the first-order spectra and responses using the tool *combine_grating_spectra*.

3. Analysis and Results

Miller et al. (2015) analyzed X-ray spectra of ASASSN-14li using the SPEX package (Kaastra et al. 1996), and reported the first direct application of the "pion" photoionization model. In this analysis, we follow an analogous procedure using updated versions of SPEX and pion (versions 3.06.01 and 1.04, respectively). Pion offers two advantages over other widely available photoionization models and packages. First, unlike external tables of photoionization spectra that are based on a fixed input spectrum, the *pion* model reads the illuminating flux and self-consistently adjusts within the process of minimizing the goodness-of-fit statistic, so that the gas is irradiated by the best-fit continuum. Second, multiple pion components can be layered—the total spectral model can be constructed so that the radially exterior absorption zones see the central engine flux after modification by interior absorption zones (see, e.g., Trueba et al. 2019).

After obtaining spectra and responses from *rgsproc*, the *trafo* package was used to convert them into the format required by SPEX. This conversion streamlines the files and makes spectral fits within SPEX much faster. We made joint fits to the RGS-1 and RGS-2 spectra over the 16–36 Å band, minimizing a Cash statistic (Cash 1979). Outside of this passband, the sensitivity of the spectra is greatly reduced. We adopted an adaptive binning scheme in order to maximize the sensitivity of the spectra: the bins in the 16–20 Å range were grouped to have a signal to noise ratio of 10.0, and the bins in the 20–36 Å range were grouped to have a signal to noise ratio of 5.0. The summed first-order Chandra LETG spectrum was grouped in the same manner and fit over the same band. All of the errors quoted in this work are based on the values of model parameters at their 1σ confidence limits.

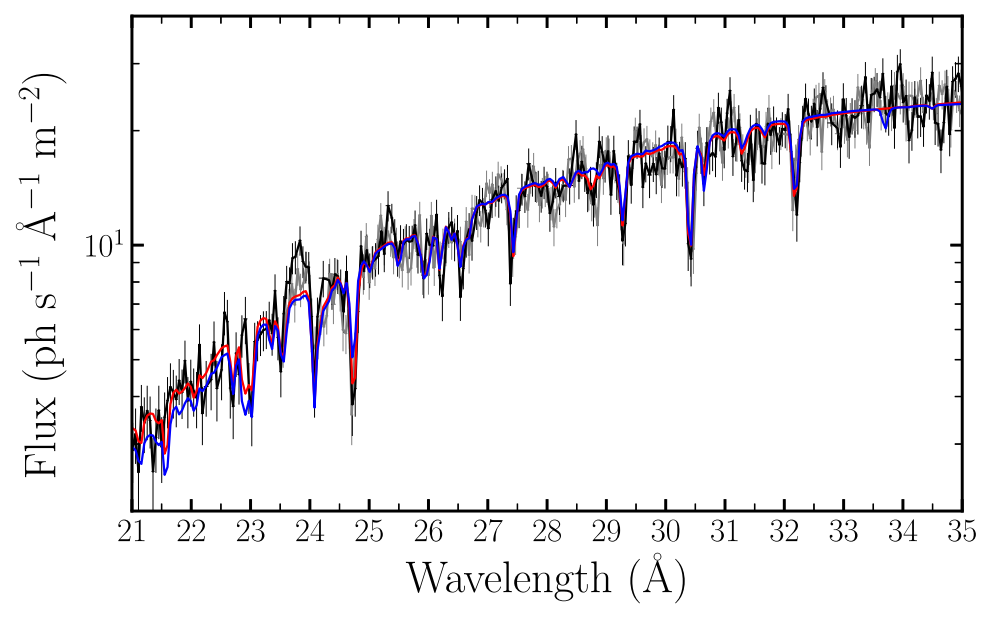


Figure 1. RGS1 (black) and RGS2 (gray) spectra of ASASSN-14li from the longest XMM-Newton observation of this TDE. The wavelength scale is shifted to the frame of the host galaxy. The model in blue (XMMs in Table 1) represents the best *pion* photoionized absorption model with solar abundances. The H-like N VII resonance line at 24.78 Å and the He-like N VII resonance line at 28.78 Å are underpredicted, while the H-like C VII resonance line at 33.73 Å is overpredicted. The model in red (XMMt in Table 1) shows the best absorption model when the abundances of carbon and nitrogen are allowed to vary. An enhanced N abundance, potentially as high as 100 times solar, provides a better fit to the N lines. Similarly, the data require that the C abundance is at most 0.4 times solar, giving $[N/C] \geqslant 2.4$. Please see the text and Table 1 for additional details.

Table 1
Spectral Models and Parameters

Parameter	XMMs	XMMf	XMMt	XMMd	CXOs	CXOt
Abundances	Solar	Frozen	Thawed	Thawed, dcpl.	Solar	Thawed
kT (eV) Norm (10 ²⁵ cm ²)	50.7 ± 0.3 5.1 ± 0.4	51.4 ± 0.4 4.4 ± 0.4	54.6 ± 0.5 2.2 ± 0.2	54.6 ± 0.5 2.2 ± 0.2	53.2 ± 0.9 2.7 ± 0.6	55.9 ± 0.9 1.7 ± 0.4
$N_{\rm H}$ (TDE, $10^{22}{\rm cm}^{-2}$) $\log \xi$ $v_{\rm rms}~({\rm km~s}^{-1})$ $v_{\rm out}~({\rm km~s}^{-1})$ $A_{\rm C}$ $A_{\rm N}$	2.6 ± 0.3 4.71 ± 0.05 86 ± 8 340 ± 30 1.0^{*} 1.0^{*}	$3.0^{+0.5}_{-0.4}$ 4.55 ± 0.07 76 ± 7 360^{+20}_{-30} 0.33^{*} 10.0^{*}	2.5 ± 0.4 4.32 ± 0.06 91 ± 8 370 ± 30 $0.0^{+0.1}$ 110 ± 20	2.5 ± 0.4 4.31 ± 0.04 91 ± 8 370 ± 30 $0.0^{0.1}, 0.0^{+0.4}$ $113^{+17}_{-15}, 109^{+17}_{-15}$	1.8 ± 0.6 4.6 ± 0.1 67 ± 14 280 ± 80 1.0^* 1.0^*	$2.0^{+0.9}_{-0.6}$ 4.4 ± 0.1 60 ± 12 330^{+70}_{-50} $0.0^{+0.4}$ 160^{+210}_{-60}
$N_{\rm H}$ (host, 10^{20} cm ⁻²)	$1.1^{+0.6}_{-0.3}$	$1.3^{+0.5}_{0.4}$	1.2 ± 0.4	1.2 ± 0.4	2.0 ± 0.9	1.4 ± 0.7
$N_{\rm H} ({\rm MW}, 10^{20} {\rm cm}^{-2})$	$4.3^{+0.4}_{-0.7}$	$3.8^{+0.4}_{-0.5}$	2.8 ± 0.4	2.1 ± 0.4	2.5 ± 0.8	1.9 ± 0.7
Flux (10 ⁻¹¹ erg cm ⁻² s ⁻¹)	3.0 ± 0.2	3.1 ± 0.3	3.5 ± 0.4	3.6 ± 0.4	2.8 ± 0.6	3.2 ± 0.8
C/ν	1547.6/641	1488.12/641	1351.2/639	1351.1/637	351.5/280	328.0/278

Note. Parameters measured from models fit to the XMM-Newton and Chandra spectra of ASASSN-14li. From top to bottom, the model parameters are arranged to reflect the light path taken from the central engine to the telescope. Ionized absorption within the central engine of the TDE was fit using the *pion* photoionization package; intervening absorption in the hot ISM of the host and Milky Way were fit using *hot*. Within the models, the blackbody emission, ionized absorption, and ISM absorption within the host were redshifted to the host value, so outflow velocities are reported relative to the host. Parameter values that are marked with an asterisk (*) were fixed within the particular model. The fit designated "XMMs" represents a joint fit to the RGS1 and RGS2 spectra with "pion" abundances fixed at solar values. The fit designated "XMMf" froze the abundances of carbon and nitrogen within *pion* to arbitrarily diminished and enhanced values. In "XMMt," the carbon and nitrogen abundances were *thawed* and varied freely. The fit designated "XMMd" allowed the abundances of carbon and nitrogen to float freely and decoupled these parameters in the RGS1 and RGS2 spectra. In the "CXOs" fit, the Chandra data were fit assuming a wind with solar abundances. Finally in the "CXOt" fit, the Chandra data were fit with the abundances of C and N *thawed*. All fluxes are quoted in the 0.1–10.0 keV band.

We initially considered the same model that is reported in Miller et al. (2015): a simple blackbody ("bb") continuum component, acted upon by local photoionized absorption ("pion") with solar abundances, absorption in the hot interstellar medium (ISM) of the host galaxy ("hot"), and

absorption in the ISM of the Milky Way (again via "hot"). The appropriate redshift was applied to all of the components acting within ASASSN-14li and its host galaxy (via *reds*). The full results of this fit are listed as model "XMMs" in Table 1 and shown in Figures 1 and 2 (in blue).

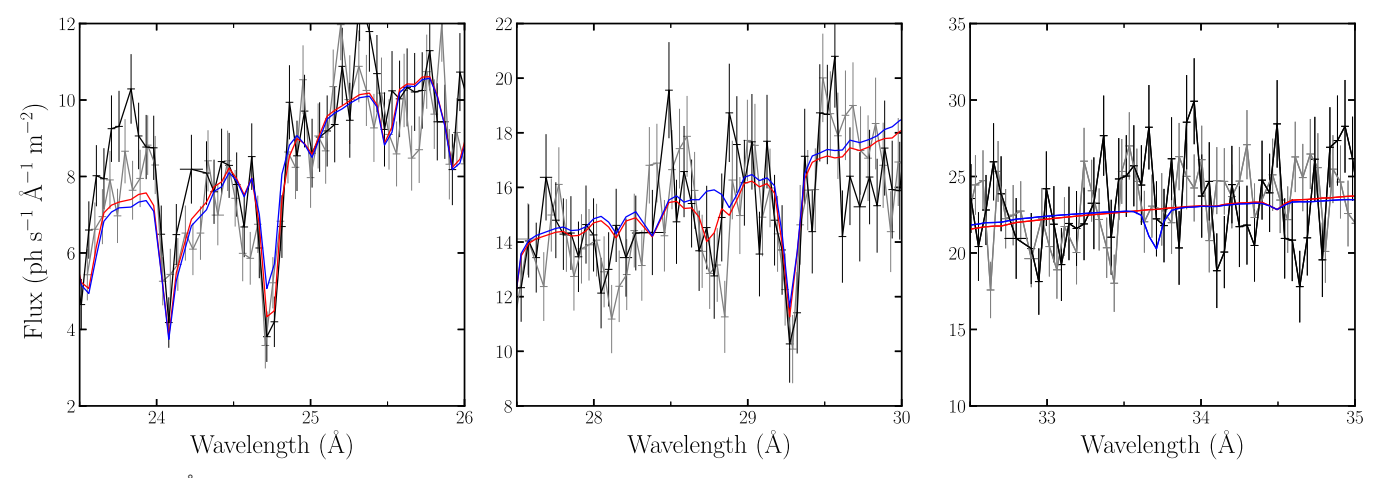


Figure 2. Narrow, 2.5 Å slices of the XMM-Newton spectra of ASASSN-14li shown in Figure 1. The RGS1 spectrum is shown in black; the RGS2 spectrum in gray. Both spectra are shifted to the host frame. The model in blue is *XMMs* with solar abundances; the model in red is *XMMt* with thawed N and C abundances, giving $[N/C] \ge 2.4$. The left panel centers the H-like N VII line at 24.78 Å, the middle panel centers the He-like N VI line at 28.78 Å, and the right panel centers the H-like C VI line at 33.73 Å.

This baseline model gives a Cash statistic of C=1547.55, for $\nu=641^\circ$ of freedom. The blackbody temperature is measured to be $kT=50.7\pm0.3\,\mathrm{eV}$, and its flux normalization is measured to be $K=5.1\pm0.4\times10^{25}\,\mathrm{cm}^2$, or a characteristic radius of $r=2.0\pm0.1\times10^{12}\,\mathrm{cm}$, and assuming that $K=4\pi r^2$. It is likely that these fiducial numbers are underestimates, since Compton scattering leads to artificially high temperatures and small emitting areas (e.g., Shimura & Takahara 1995). The blackbody temperature is formally consistent with the value reported in Miller et al. (2015), while the emitting area is slightly higher. The inferred luminosity of the source is $L_X=2.8\pm0.2\times10^{44}\,\mathrm{erg}\,\mathrm{s}^{-1}$ (0.1–10 keV).

The measured outflow velocity is $v = -340^{+20}_{+40}$ km s⁻¹, with a turbulent velocity of $\sigma = 86 \pm 8$ km s⁻¹. The outflow column density is measured to be $N_{\rm H} = 2.6 \pm 0.3 \times 10^{22}$ cm⁻², with an ionization given by $\log \xi = 4.71 \pm 0.05$. Relative to the outflow parameters reported in Miller et al. (2015), the outflow velocity is approximately 50% higher, the turbulent velocity is broadly consistent, the column density is approximately 2 times higher, and the ionization is about 3 times higher. If the ionization parameter is frozen to the value measured in the prior fits, $\log \xi = 4.2$, the fit statistic increases to C = 1615.55 ($\Delta C = 68$, $\Delta \nu = 1$), strongly indicating that the change in values is real. The differences are likely due to improvements in the atomic physics that is included in the *pion* model, and improved weighting.

Next, we considered three potential improvements to this model: (1) nonsolar values of the abundances of C and N within this single wind zone, (2) a second, faster, more central wind zone with solar abundances, and (3) two wind zones with nonsolar but linked values for the abundance of C and N.

When the abundances of C and N are allowed to float in the single wind zone, the fit statistic improves to C=1351.2, for $\nu=639^\circ$ of freedom (or $\Delta C=-196.28$, for $\Delta \nu=-2$; see model *XMMt* in Table 1, and model in red in Figures 1 and 2 and the discussion below). When the abundances of C and N are fixed at solar values but a faster, radially interior wind zone is added, the fit statistic improves to C=1490.41, for $\nu=639^\circ$ of freedom (or $\Delta C=-57.14$, for $\Delta \nu=-2$). In this fit, the velocity width of the fast absorber was constrained to be 10% of its outflow velocity, in order to keep the fast zone from locking onto the narrow lines that might be better associated with slower gas,

or very broad features that might not be tied to the flow. The nominal outflow velocity is $v = -24,000 \pm 1000 \, \mathrm{km \, s}^{-1}$. The best overall fit is achieved when two wind zones are included, with linked but variable values for the abundance of C and N. This model achieves C = 1343.48, for v = 637 ($\Delta C = -204.07$, for $\Delta v = -4$).

Most of the improvement in the this model comes from allowing C and N to have nonsolar abundances, and evidence for a very fast wind is marginal. Applying the Akaike information criterion (AIC) as implemented by Emmanoulopoulos et al. (2016) and judging the improvements in terms of ΔAIC , the abundance variations are highly significant whereas the addition a faster outflow is not statistically significant ($\Delta AIC < 2$). In all subsequent fits, and in all fits listed in Table 1, we focused on single-zone wind models and the role of abundances.

In model *XMMf*, the abundances of carbon and nitrogen were fixed to arbitrary but plausible values (based on Mockler et al. 2022), in order to make an initial examination of the sensitivity of the data to changes in the abundance. We set $A_{\rm C}=0.3$ and $A_{\rm N}=10$. This model produced a statistically significant improvement over *XMMs* with solar abundances for all elements: C=1488.12, for $\nu=641^{\circ}$ of freedom ($\Delta C=-59.43$, for $\Delta \nu=0$). We next *thawed* the abundances of carbon and nitrogen to vary freely within the fit (formalizing the exploratory fit made previously). Model *XMMt* finds a carbon abundance of $A_{\rm C}=0.0^{+0.1}$, and a nitrogen abundance of $A_{\rm N}=110\pm20$ (1σ errors). This model represents another statistically significant improvement: C=1351.2, for $\nu=639^{\circ}$ of freedom ($\Delta C=-196.35$, for $\Delta \nu=-2$).

These results are formally consistent with a carbon abundance of zero. This reflects a limitation of the data, not a physical reality. In far more sensitive data, it is likely that the H-like C line would be detected, and a formal lower limit would be obtained. While a formal measurement of [N/C] with attendant errors is not possible with these data, we can report a lower limit. Taking the lower limit for nitrogen abundance relative to solar, $A_N = 90$, and the upper limit for carbon, $A_C = 0.1$, we obtain a lower limit of $[N/C] \geqslant 3.0$. Given the extremity of this limit, we next undertook a set of additional fits to understand if the inferred abundance pattern is influenced by

any instrumental issues, and report limits on [N/C] in the same manner.

We first decoupled the abundances of carbon and nitrogen between the RGS1 and RGS2 spectra. This modification tests the possibility that the extreme abundances are driven by an anomaly in one or both instruments that coincide with the key lines. The "XMMd" column in Table 1 lists the abundances derived from each instrument. The upper limit on the abundance of carbon derived in the RGS2 spectrum is 4 times higher than that derived in the RGS1 spectrum ($A_C \leq 0.4$ versus $A_{\rm C} \leq 0.1$). The constraints derived on the nitrogen abundance in each spectrum are closely consistent. If we conservatively consider the less constraining limit on $A_{\rm C}$, our results indicate $[N/C] \ge 2.4$. The 3σ upper limits on the carbon abundances for RGS 1 and RGS2 are $A_C \le 1.3$ and $A_C \le 1.6$, respectively. For both RGS1 and RGS2, the measured nitrogen abundances and associated 3σ errors are $A_{\rm N}=110^{+60}_{-40}$. In short, solar abundances of carbon are allowed within 3σ , but much higher abundances of nitrogen are still required.

The fits to the Chandra spectrum are listed in columns "CXOs" and "CXOt" in Table 1, designated to correspond to the fits made to the XMM-Newton spectra with solar and thawed abundances. The Chandra spectrum is less sensitive than the XMM-Newton spectra, but these fits serve as a useful check since the instrument profile is independent (including background, calibration, systematic errors, etc.). Again, the fit with variable abundances is a significant improvement over the fit with solar abundances ($C/\nu = 328.0/278$; versus $C/\nu = 351.5/280$, or $\Delta C = -23.5$, for $\Delta \nu = -2$). The upper limit on the C abundance is $A_{\rm C} \le 0.4$, and the N abundance is measured to be $A_{\rm N} = 160^{+210}_{-60}$. Nominally, then, $[{\rm N/C}] \ge 2.4$. Given that independent instruments both prefer a subsolar C abundance and elevated N abundance, and also given the similarity of the constraints, this extreme ratio limit may be robust. We additionally note that extending the Chandra LETG spectrum to 60 Å does not alter the [N/C] ratio limit that is inferred.

We also examined whether or not the assumed continuum model influences the abundance ratio limit. The true continuum flux may be that of an accretion disk, potentially modified by relativistic effects and Comptonization (e.g., Mummery & Balbus 2020; Wen et al. 2020, 2023). Over a narrow passband and at modest sensitivity, these effects cannot be detected. However, it is worth investigating if the slightly different continuum produced by a multitemperature disk model provides any improvement in the Cash statistic, or in the derived abundances. To this end, we replaced the simple blackbody in models *XMMf* and *XMM* in Table 1, with the *dbb* model within SPEX. This model is based on a Shakura–Sunyaev disk (Shakura & Sunyaev 1973); it includes a torquefree inner boundary condition, and its free parameters include the characteristic disk temperature and emitting area.

The fits with dbb produce slightly worse fits than those with the simple blackbody when the C and N abundances are frozen at solar values: C=1569.1, for $\nu=642^{\circ}$ of freedom, whereas the simple blackbody achieved C=1547.6, for $\nu=641$. This model gives a disk temperature of $kT=0.12\pm0.01$ keV, and an emitting area of $K=1.8\times10^{24}$ cm². When dbb replaces the simple blackbody within model XMMt, wherein the abundances of C and N are allowed to vary, a statistically equivalent fit is achieved. Importantly, however, the same abundance limit and measurement result: $A_{\rm C}=0.0^{+0.1}$, and $A_{\rm N}=120^{+16}_{-14}$. This

strongly indicates that the derived abundance ratio limit does not depend on the specific continuum model assumed.

Finally, we note that none of the fits detailed in this section are formally acceptable. Despite this, the changes in the fit statistic owing to model changes and enhancements are meaningful, and the direct comparisons yield physical insights. The absence of a statistically acceptable model is typical of line-rich high-resolution X-ray spectra, wherein even sophisticated models necessarily offer an imperfect description of a complex physical scenario. For instance, in recent fits to RGS spectra from the Seyfert-1 AGN 3783, Mao et al. (2019) only achieve a fit statistic of C = 6092, for $\nu = 2505^{\circ}$ of freedom, despite many layers of ionized absorption and a combination of broad and narrow emission lines.

4. Discussion

We have reanalyzed the most sensitive high-resolution X-ray spectra obtained from ASASSN-14li, with a novel focus on key elemental abundances. The spectra can be described using two zones with a wide separation in velocity, but a single zone with nonsolar abundances is strongly preferred. We find that a model that assumes solar abundances for all elements underfits He-like and H-like N absorption lines, and overpredicts the strength of the H-like C line (see Table 1 and Figures 1 and 2). Allowing for potential differences between the RGS1 and RGS2 spectra in the region of the H-like C line, the XMM-Newton data still require $[N/C] \geqslant 2.4$; the Chandra spectrum of ASASSN-14li independently verifies this ratio limit. The same limit is obtained when a disk blackbody continuum is assumed instead of a simple blackbody. Here, we discuss the implications of this finding for our understanding of TDEs.

The CNO cycle operating in stellar interiors leads to core material that is nitrogen-rich and carbon-deficient relative to material unprocessed by nuclear burning (Iben 1964, 1967; Lambert & Ries 1977, 1981). The rate of CNO processing is regulated by the Coulomb barrier for proton capture onto CNO nuclei and consequently has a strong temperature dependence. Increasing the core temperature with stellar mass means that CNO processing is more efficient and more extensive in higher mass stars, leading to greater N enrichment and C depletion (Iben 1964).

Kochanek (2016) and Gallegos-Garcia et al. (2018) explored the potential for this processing to reveal the masses of disrupted stars. Mockler et al. (2022) recently studied this issue in detail, finding that stars more massive than $M=1.3\,M_\odot$ are required to give $[{\rm N/C}] \geqslant 1.5$. Based on stellar demographics, the fact that massive stars live for a relatively short time, and the properties of stars observed in nuclear star clusters, Mockler et al. (2022) conclude that the stars more massive than $M=3\,M_\odot$ are not likely to be disrupted at an significant rate.

The fits to the UV spectrum of ASASSN-14li require $[N/C] \geqslant 1.5$ (Yang et al. 2017). The more extreme abundance ratio in our fits to the X-ray data of ASSASN-14li nominally points to a star at the limit of the range considered by Mockler et al. (2022), or potentially an even more massive star. If the cluster of young, massive stars surrounding Sgr A* (e.g., Lu et al. 2013) is typical of the nuclear environment in other galaxies, then it is possible that a sizable fraction of disruptions involve relatively massive stars.

In particular, if the diffuse UV and X-ray gas have different abundance patterns—potentially corresponding to different parts of the stellar interior—their relative position within the

accretion flow may be a window on the disruption itself. However, such disparities are not anticipated by theoretical treatments that address mixing (e.g., Law-Smith et al. 2019), and we note that the narrow UV and X-ray absorption lines in ASASSN-14li have fully consistent blueshifts (Miller et al. 2015; Cenko et al. 2016). The broadening of the N IV] emission line in the Hubble UV spectrum of ASASSN-14li suggests a production radius of about 150 AU, or $r \simeq 2.3 \times 10^{15}\,\mathrm{cm}$ (Cenko et al. 2016). The gas exhibiting H-like and He-like N absorption in X-rays is constrained to lie within $r \leqslant 3 \times 10^{15}\,\mathrm{cm}^{-2}$ through variability (Miller et al. 2015).

Even with realistic mixing between layers at disruption, a full disruption of a $M \simeq 3 M_{\odot}$ star may not be able to reproduce the abundances measured in this study (see Law-Smith et al. 2019). It is possible that the environment close to massive black holes can lead to mergers, via the "eccentric Kozai-Lidov" mechanism (Stephan et al. 2016). Such stars could resemble G2 and represent a young, massive population that is not possible in less extreme environments. But, more mundane explanations are also possible. Even within solar-mass stars, nitrogen is more abundant than carbon close to the core. If the disrupted star had previously been partially stripped of its envelope, exposing more processed material at the point of disruption, this could potentially account for at least some of the observed abundance pattern. Key facets of the nuclear environment could also play a role: McKernan et al. (2022) note that the envelopes of evolved stars can be stripped by ram pressure in AGN disks. A potential shortcoming of this alternative is that a strong Ly α line was detected in ASASSN-14li (Cenko et al. 2016), signaling that at least some of the stellar envelope was retained prior to the disruption event. If stripping is not viable as a fully independent alternative to the massive stellar interpretation, it may be that a degree of stripping contributed to the extreme abundance pattern.

The theoretical treatments of TDEs did not anticipate the discovery of X-ray winds with properties like Seyfert warm absorbers. In the classical picture of TDEs, approximately half of the stellar mass is expected to be ejected at much greater speeds, $v \ge 10^4 \, \mathrm{km \, s^{-1}}$ (e.g., Rees 1988). The variability in the wind observed in ASASSN-14li pointed to an absorption radius consistent with the broad line region (BLR) in Seyferts (Miller et al. 2015), and it is notable that the best optical spectra of TDEs now also exhibit a BLR (e.g., Hung et al. 2020). In this sense, UV and X-ray winds consistent with Seyfert BLRs might be expected to be common in TDEs. However, it was not possible to completely exclude the possibility that the X-ray wind could be tied to *prior* low-level AGN activity within the nucleus.

Studies that utilize optical emission lines from the BLR in AGN generally find supersolar metallicities (e.g., Ferland et al. 1996; Dietrich et al. 1999, 2003). However, several effects can complicate such inferences. In principle at least, wind absorption lines offer the chance to make absolute measurements with direct ratios to hydrogen. Combining simultaneous UV and X-ray wind spectra of Mrk 279, for instance, Arav et al. (2007) found that the abundances of C, N, and O are elevated by factors of 2.2 ± 0.7 , 3.5 ± 1.1 , and 1.6 ± 0.8 (respectively). This pattern differs markedly from the extreme nitrogen to carbon ratio limit inferred in ASASSN-14li. As a result, the wind observed in ASASSN-14li can only be

consistent with material that originated in a single, disrupted star.

Mummery & Balbus (2020) fit the X-ray and UV decay curves of ASASSN-14li with a relativistic thin disk model, and find that the accreted mass was likely $M \sim 0.016 M_{\odot}$, implying a disrupted stellar mass of $M \sim 0.032 M_{\odot}$. In contrast, Wen et al. (2020) fit the X-ray decay with slim accretion disk models that include advection and a spectral hardening factor, and find that a disrupted stellar mass of $M \ge 0.34 M_{\odot}$ is implied. It is possible that these low disrupted stellar mass estimates can be reconciled with the relatively high mass inferred via abundances if the accretion disk formation efficiency is very low (see, e.g., Dai et al. 2015; Piran et al. 2015; Shiokawa et al. 2015), so that most of the disrupted stellar mass is lost and/or waiting to accrete even at very late times. However, both treatments omit the role of outflows in assessing the total accreted mass; though, both winds and jets are clearly present in ASASSN-14li (e.g., Miller et al. 2015; Alexander et al. 2016). A slim disk with strong advection and correspondingly lower efficiency for converting \dot{M} into radiation would also lead to higher estimates of the accreted mass and disrupted stellar mass. Additionally, Wen et al. (2023) note that, if the UV emission observed in ASASSN-14li soon after its discovery is due to shocks, a disrupted stellar mass in excess of $M \ge 1.4 M_{\odot}$ is required for their minimum preferred black hole mass. Most importantly, perhaps, modeling of the UV light curve of ASASSN-14li points to a disruption about 35 ± 3 days before its discovery, during a time when it was unobservable from the ground (Miller et al. 2015; Holoien et al. 2016). This period would likely correspond to the most highly super-Eddington part of the TDE, and would add greatly to the accreted mass and the corresponding disrupted stellar mass.

The tools and techniques that have permitted discoveries in ASASSN-14li are essentially those developed in the study of the brightest Seyfert AGN. However, the Seyfert-like flux of ASASSN-14li is the result of its proximity. It is now clear that the rate of highly proximal TDEs is relatively low, so few cases will reach a Seyfert-like flux of $F = 1.0 \times 10^{-11} \text{ erg cm}^{-2} \text{ s}^{-1}$ in soft X-rays. A much larger set of TDEs are at least an order of magnitude fainter. Given that long observations are needed to perform detailed spectroscopic and variability studies in bright TDEs and Seyferts using Chandra, XMM-Newton, and NuSTAR, it is clear that additional progress will require more sensitive instruments. The Athena/X-IFU will provide a resolution of 2 eV across the 0.3-10.0 keV passband, and an effective area nearly 2 orders of magnitude higher than that of the RGS in the 0.3-0.5 keV band where the crucial N and C lines are found (Barret et al. 2023). The proposed Arcus Probe mission will deliver even higher resolution at long wavelengths, and simultaneous UV coverage (Smith et al. 2022).

Acknowledgments

We thank the anonymous referee for comments that improved this manuscript. We acknowledge helpful discussions with Elena Gallo, Jelle Kaastra, and Jelle de Plaa. We note that the "wicker basket" scenario referenced in this work may have been coined by Martin Rees at a conference in his honor at the University of Cambridge in 2017.

ORCID iDs

Jon M. Miller https://orcid.org/0000-0003-2869-7682

```
Brenna Mockler  https://orcid.org/0000-0001-6350-8168 Enrico Ramirez-Ruiz  https://orcid.org/0000-0003-2558-3102
```

Paul A. Draghis https://orcid.org/0000-0002-2218-2306
Jeremy J. Drake https://orcid.org/0000-0002-0210-2276
John Raymond https://orcid.org/0000-0002-7868-1622
Mark T. Reynolds https://orcid.org/0000-0003-1621-9392
Abderahmen Zoghbi https://orcid.org/0000-0002-0572-9613

References

```
Alexander, K., Berger, E., Guillochon, J., Zauderer, B. A., &
   Williams, P. K. G. 2016, ApJL, 819, L25
Arav, N., Gabel, J., Korista, K., Kaastra, J., Kriss, G., et al. 2007, ApJ,
   658, 829
Barret, D., Albouys, V., den Herder, J.-W., et al. 2023, ExA, 55, 373
Cash, W. 1979, ApJ, 228, 939
Cenko, S. B., Cucchiara, A., Roth, N., et al. 2016, ApJL, 818, L32
Dai, L., McKinney, J. C., & Miller, M. C. 2015, ApJL, 812, L39
Dietrich, M., Appenzeller, I., Hamann, F., et al. 2003, A&A, 398, 891
Dietrich, M., Wagner, S., Courvoisier, J., Bock, T., & North, H. 1999, A&A,
  351, 31
Emmanoulopoulos, D., Papadakis, I. E., Epitropakis, A., et al. 2016, MNRAS,
  461, 1642
Ferland, G., Baldwin, J., & Korista, K. 1996, ApJ, 461, 683
Gallegos-Garcia, M., Law-Smith, J., & Ramirez-Ruiz, E. 2018, ApJ, 857, 109
Gezari, S. 2021, ARA&A, 59, 21
Guillochon, J., Makukian, H., & Ramirez-Ruiz, E. 2014, ApJ, 783, 23
Guillochon, J., & Ramirez-Ruiz, E. 2015, ApJ, 809, 166
Hickox, R., Jones, C., Forman, W., et al. 2009, ApJ, 686, 891
Holoien, T., Kochanek, C., Prieto, J., et al. 2016, MNRAS, 455, 2918
Hung, T., Foley, R., Ramirez-Ruiz, E., et al. 2020, ApJ, 903, 31
Iben, I. 1964, ApJ, 140, 1631
```

```
Iben, I. 1967, ApJ, 147, 624
Jose, J., Guo, Z., Long, F., et al. 2014, ATel, 6777, 1
Kaastra, J., Mewe, R., & Nieuwenuijzen, H. 1996, in UV and X-ray Spectroscopy
  of Astrophysical Plasmas, ed. K. Yamashitea & T. Watanabe, 411
Kara, E., Miller, J. M., Reynolds, C. S., & Dai, L. 2016, Natur, 535, 388
Kochanek, C. S. 2016, MNRAS, 458, 127
Lambert, D., & Ries, L. 1977, ApJ, 217, 508
Lambert, D., & Ries, L. 1981, ApJ, 248, 228
Law-Smith, J., Guillochon, J., & Ramirez-Ruiz, E. 2019, ApJL, 882, L25
Lu, J. R., Do, T., & Ghez, A. M. 2013, ApJ, 764, 155
Mao, J., Mehdipour, M., Kaastra, J. S., et al. 2019, A&A, 621, 99
McKernan, B., Ford, K. E. S., Cantiello, M., et al. 2022, MNRAS,
   514, 4102
Miller, J. M., Kaastra, J., Miller, M., et al. 2015, Natur, 526, 542
Mockler, B., Twum, A., & Auchettl, K. 2022, ApJ, 924, 70
Mummery, A., & Balbus, S. A. 2020, MNRAS, 492, 5655
Pasham, D., Remillard, R., Fragile, P., et al. 2019, Sci, 363, 531
Phinney, E. S. 1989, in IAU Symp. 136, The Center of the Galaxy, ed.
   M. Morris (Dordrecht: Kluwer Academic), 543
Piran, T., Svirski, G., Krolik, J., Cheng, R. M., & Shiokawa, H. 2015, ApJ,
   806, 164
Rees, M. 1988, Natur, 333, 523
Reis, R., Miller, J. M., & Reynolds, M. T. 2012, Sci, 337, 949
Roth, N., Rossi, E. M., & Krolik, J. 2020, SSRv, 216, 114
Shakura, N., & Sunyaev, R. 1973, A&A, 24, 337
Shimura, T., & Takahara, F. 1995, ApJ, 445, 780
Shiokawa, H., Krolik, J. H., Cheng, R. M., Piran, T., & Noble, S. C. 2015, ApJ,
Smith, R. K., Bautz, M., Bregman, J., et al. 2022, Proc. SPIE, 12181, 1218121
Stephan, A., Naoz, S., & Ghez, A. 2016, MNRAS, 460, 3494
Trueba, N., Miller, J. M., & Kaastra, J. 2019, ApJ, 886, 104
Wen, S., Jonker, P. G., Stone, N. C., van Velzen, S., & Zabludoff, A. I. 2023,
      IRAS, 522, 1155
Wen, S., Jonker, P. G., Stone, N. C., Zabludoff, A. I., & Psaltis, D. 2020, ApJ,
Yang, C., Wang, T., & Ferland, G. 2017, ApJ, 846, 150
```